# Charge exchange ion losses in Saturn's magnetosphere

A. Sontag[1,2], G. Clark[2], P. Kollmann[2]

[1] University of Pennsylvania, Philadelphia, PA
[2] Johns Hopkins University Applied Physics Laboratory, Laurel, MD

Corresponding author: George Clark (george.clark@jhuapl.edu)

## Key Points

- Survey of suprathermal proton and water group ions in Saturn's magnetosphere show strong variability at <1MeV.
- Data comparisons to a physical model suggest that charge exchange plays a key role in removing suprathermal ions between 5 and 15 $R_S$.
- This result is important for better understanding ion-neutral interactions and loss processes in Saturn's magnetosphere.

## Abstract

While various source and loss processes have been proposed for ions in Saturn's magnetosphere, it is not yet well understood what role they play in different regions. In this study, we use a physical model of charge exchange to predict how proton and water group ion intensity profiles evolve over time and compare the results to MIMI/CHEMS measurements collected during the Cassini mission. First, we divide the CHEMS data into inbound and outbound half-orbit segments, and create intensity profiles for 3-220 keV $H^+$ and $W^+$ ions between 5 and 15 Saturn radii, then using the inbound half-orbits as initial conditions, we find qualitative similarities between measured and predicted outbound intensity profiles. This result is important because it provides strong evidence that charge exchange is the dominant loss process for these species in this region. The observed rate of charge exchange also presents information on the density of Saturn's neutral torus. We suggest that data-model discrepancies in the water group ions may be an indication of a significant presence of ions with the water group mass that are multiply charged.

## 1. Introduction

The first studies of charged particles in Saturn's magnetosphere date back to the 1980s, using data collected by the Pioneer 11 mission (e.g., Van Allen et al., 1980; Fillius et al., 1980) and subsequent Voyager missions (e.g., Krimigis et al., 1981, 1982). The source of suprathermal ions was poorly understood until Cassini began orbiting Saturn in 2004. Ions are created at low energies in the inner magnetosphere when material erupted from Enceladus' plumes is ionized (Delamere et al., 2007) and picked up by the magnetic field. They then begin moving radially outward due to injection processes driven by the centrifugal force of their drift motion. Those same injections also bring ions from larger distances inward, during which they are accelerated up to keV energies. There is still much to learn regarding the role of injection processes, but various studies suggest that they may be due to magnetic flux tube interchange caused by gradients in the

magnetosphere plasma (Southwood & Kivelson, 1987; Morfill et al., 1993). A good approximation for this energy gain process assumes that the particles' motion is invariant under timescales slower than their bounce-motion and that their energy increases under conservation of the invariants associated with bounce and gyration. This assumption is able to reproduce the data well (Hood, 1983; Clark et al., 2014) and is directly supported by observations of the electron cutoff energy and ion temperature (Dialynas et al., 2010; Kollmann et al., 2018).

Saturn's inner-to-middle magnetosphere is dominated by neutral gases instead of plasma (Krupp et al., 2018), different from the other planets on which charge exchange has been studied (Delamere et al., 2007). Plumes on its geologically active moon Enceladus are constantly adding between 100 and 1000 kg/s of water vapor to what is known as Saturn's neutral torus (Teolis et al., 2017). Photolysis breaks these $H_2O$ molecules down into OH, O, and H neutrals (Smith et al., 2010), which permeate the magnetosphere in the vicinity of Enceladus's orbital path due to their long lifetimes (Melin et al., 2009). From Cassini in-situ measurements and modeling (e.g. Smith et al., 2010; Fleshman et al., 2012), we know that the main neutral torus constituent near Enceladus (~4 $R_S$) is $H_2O$, but rapidly becomes OH and O with increasing distance from the icy satellite. Plots of neutral density as a function of radial distance can be found in Figures 5 and 10B, and will be discussed more thoroughly in section 4.4.

We define water group ions as $H_{0\text{-}3}O^+$ and abbreviate them as $W^+$. Figure 1 shows the mission-averaged profiles of proton and water group fluxes as a function of radial distance and energy, measured by the Cassini CHEMS instrument (see section 2.1 for description). Both water group ions and protons exhibit an increase in flux from beyond 15 $R_S$ ($R_S$ is the Saturn radius) inward until ~9 $R_S$, then decreasing until ~5 $R_S$. Higher energy particles (yellow in Fig. 1) reach to smaller distances than lower energy particles (blue).

Because of this neutral torus domination, it is generally assumed that charge exchange—a process involving the transfer of electrons between ions and neutral particles—is responsible for the decrease in ion intensity inward of ~9 $R_S$ shown in Figure 1 (Paranicas et al., 2008). However, it is not clear how this loss process can explain the observed similarities and differences in radial and energy gradients between protons and water group ions. Many previous studies of charge exchange in Saturn's magnetosphere have not addressed this phenomenon. Jurac et al. (2005) create a physical model of plasma-neutral interactions, but their focus on inferring the neutral torus density leads them to ignore the temporal variations in plasma flux. Fleshman et al. (2010) create a similar model and focus on the ion lifetimes, but only within the immediate vicinity of Enceladus. The energy dependence of the $H^+$ distribution in Figure 1 is consistent with the charge exchange cross section of protons (Kollmann et al., 2015) that rapidly decreases at around 100 keV. The oxygen cross section, however, stays relatively constant (discussed more below and shown in Fig. 12), so the apparent similarity between protons and oxygen is surprising and the motivating feature for this study: Why do the light and heavy ions behave differently here? Our study aims to explain the discrepancy between proton and water group ion measurements by exploring the dominant gain and loss processes for ions between 5 and 15 $R_S$, in order that we might better understand the plasma environment around Saturn.

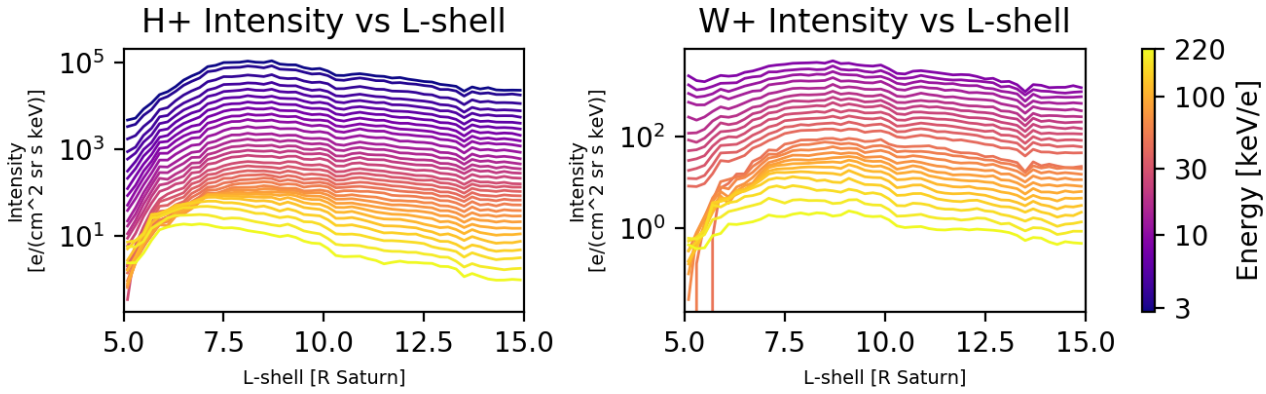


*Figure 1: Radial intensity profiles of H+ and W+ ions from ~3 to 220 keV/e. Lines are colored based on their energy, mapped according to the color bar on the right. Water group ions and protons experience different radial gradients inward of ~8 $R_S$, and these differences vary with energy, motivating the exploration done in this study.*

## 2. Methodology

In this section, we analyze the $H^+$ and $W^+$ intensities measured by CHEMS and divide them into segments based on the inbound and outbound parts of Cassini's orbit. We find that these orbital profiles permit a qualitative categorization scheme, and we use these categories to hypothesize that charge exchange is the driving loss process of the observed variability. To test our hypothesis, we develop a physical model of charge exchange and compare its predictions to the measured data.

### 2.1 Data Analysis

Ion measurements in this study were obtained from the Charge-Energy-Mass-Spectrometer (CHEMS) on board the Cassini spacecraft – a Saturn orbiting mission from 2004 to 2017. CHEMS is an instrument designed to characterize the suprathermal ion population in Saturn's magnetosphere by measuring the charge state, energy, mass and angular distributions of ions (Krimigis et al., 2004). Incident ions are first selected by their energy-per-charge in CHEMS' front-end electrostatic analyzer and then pass through a series of foils comprising a time-of-flight chamber (TOF) before depositing their residual energy into a solid-state detector (SSD). The three-part system, i.e., E/Q, TOF and deposited energy in the SSD, provides clean triple coincidence measurements of the foreground ion populations and allows for energy, mass and charge state determination. CHEMS is not able to resolve the masses of $H_nO^+$ for different n-values, which is why we refer to all of them as $W^+$. For charge exchange calculations, we assume that $W^+$ is dominated by $O^+$. CHEMS is able to uniquely identify various minor species including $W^{2+}$, but we limit our analysis to $H^+$ and $W^+$ for simplicity.

Pitch angle distributions are then derived by including measurements of the local vector magnetic field from the Cassini magnetometer (Dougherty et al., 2004). CHEMS is designed to measure an energy range from ~3 – 220 keV/e with a mass-per-charge range

of 1 – 80 amu/e. Additionally, CHEMS has three look directions which each have a field of view (FoV) of ~4° × 53°. While CHEMS provides only coarse pitch angle distributions, the Cassini spacecraft performs quasi-periodic maneuvers or spins about the S/C z-axis during which the instruments can measure more complete pitch angles.

As mentioned previously, the Cassini mission was in orbit from 2004 to 2017. During this epoch the spacecraft traversed a large volume of Saturn's magnetosphere through a combination of equatorial and polar orbits. Cassini spent the majority of its mission inside 40 $R_S$ and at all local times for nearly complete coverage of the region where energetic particles are likely interacting with the Enceladus gas cloud. Figure 2A illustrates the complete mission orbital profile mapped onto the equatorial plane, showing the radial and local time coverage of the measurements presented in this study. Figure 2B is an illustration of one example orbit representative of the data used for the model comparisons in the next section. The different colors in Figure 2B depict the inbound and outbound segments of the orbit, which we also refer to as "half-orbits" in this paper.

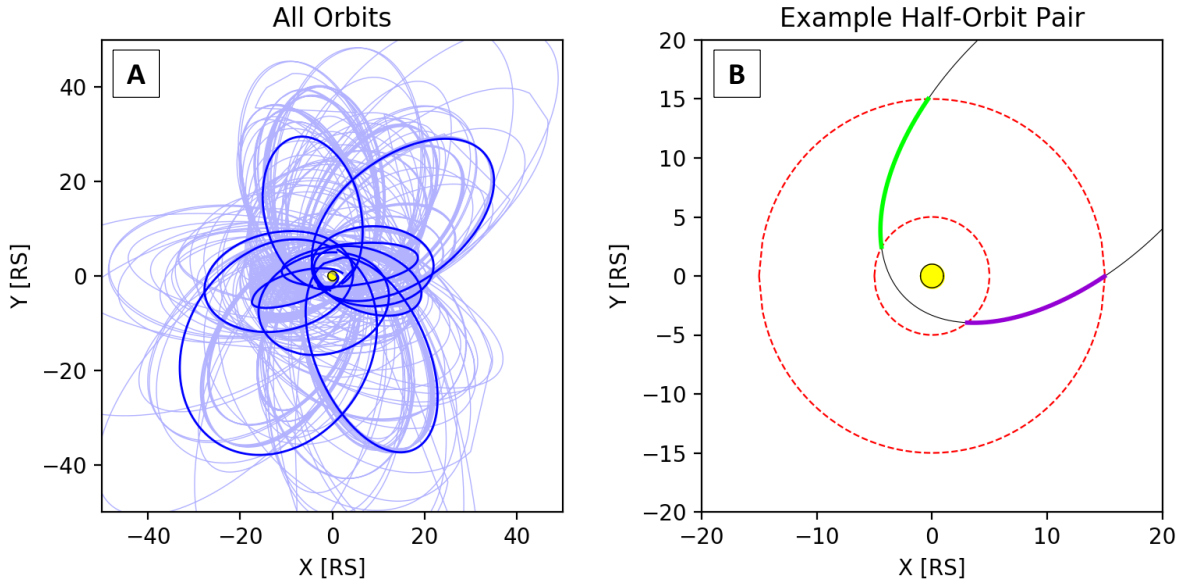


*Figure 2: A) Plot of Cassini's complete mission orbital profile mapped onto the equatorial plane. Most orbits are plotted in light blue, but every 30th orbit is plotted in bold. B) One example of a half-orbit pair. The red dashed lines show L=5 and L=15 $R_S$, inside of which is the region of interest for this study. The thin black line shows the full example orbit. The bold green segment is the inbound portion of interest, and the bold purple segment is the outbound portion of interest. This orbit corresponds to the intensity profiles shown in Figure 8, and took place between 2011.725 and 2011.775.*

A useful diagnostic in understanding how energetic particles are sculpted in a magnetosphere is simply looking at their energy and spatial profiles. In Figure 3 we show the color-coded differential intensities of ions organized by their measured energy and L-shell. Note that energies below 8.35 keV/e are not included in the $W^+$ profile because CHEMS is unable to distinguish between these and other ions at any lower energies (Vandegriff et al., 2018). This limitation of the energy range is indicated by the green box in Figure 3. The example shown in Figure 3 is averaged over the entire mission (2004 – 2017), which is why the spectrograms appear relatively uniform. Mission-averaging is helpful for models of magnetospheric equilibrium, such as those produced by Richardson et al. (1990) and Persoon et al. (2009), but it masks physical processes by smearing out

any local and temporal fluctuations. This uniform picture is our motivation for dividing Cassini's trajectory into small segments based on its orbital position in an effort to unearth spatially localized processes occurring on shorter timescales. By cutting the CHEMS data at the local minima and maxima of Cassini's distance from Saturn, we define half-orbit trajectory segments. For each half-orbit we create intensity profiles for $H^+$ and $W^+$ akin to that in Figure 3, but now averaged over a much shorter timescale. Half-orbit intensity profiles retain for the most part the clarity afforded by the mission-averaged data, while also revealing the dominant gain and loss processes in this region. Examples of such profiles can be seen in Figure 4.

Cassini made 293 full orbits around Saturn during its mission, yielding 586 half-orbit segments. The time spent on each half-orbit varies based on the mission phase, but the majority fall between 3.5 and 11 (Earth) days. This segmentation scheme is helpful because the timescales do not differ too much between half-orbits, and they change slowly between mission phases. The different segments are also physically meaningful: each whole orbit is divided into its "inbound" and "outbound" components (see Figure 2B), such that the set of half-orbits alternate between subsequent inbound/outbound pairs. By definition, this means that Cassini's radial distance from Saturn is a monotonic function of time for each half-orbit. In most cases this translates to a monotonic function of L-shell versus time as well, but there are occasional turnarounds near the fringes due to the dipole field shape at high latitudes. The majority of the half-orbits have no turnarounds.

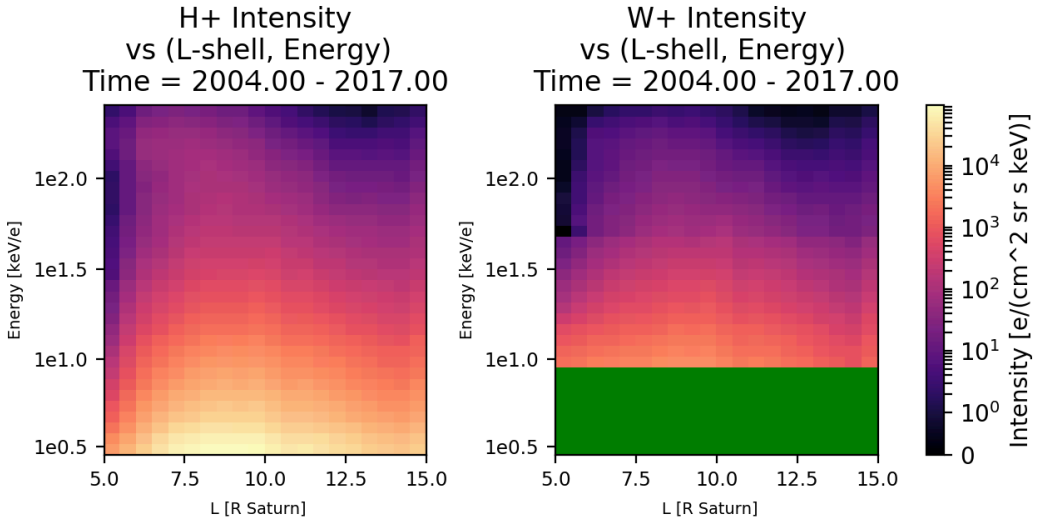


*Figure 3: Mission-averaged intensity profiles versus energy and L-shell from the CHEMS data. Differential intensity for an E,L region is denoted by color, according to the color bar on the right. Intensity is mapped to color based on a "symlog" scale, which is logarithmic for values greater than 1 and linear for values between 0 and 1 such that regions with no intensity can be displayed alongside regions with intensities that vary by multiple orders of magnitude (see section 2.2 for derivation).*

From this large pool of half-orbit profiles, we identify 6 qualitative categories into which significant numbers of half orbits fall. These categories can be seen in Figure 4. Category 1 includes the highest population of ions. It is composed of predominantly uniform profiles, meaning high intensity at low energies moving smoothly into medium intensity at higher energies, with few if any regions of no intensity. Relatively high intensities are

found until the inner boundary at $L = 5$. For $W^+$ it is permissible to have intensity dropouts in the high energy, low L region.

Categories 2a, 3a, and 4 have smaller and smaller ion populations. We will interpret this decay as being a result of ongoing charge exchange. Category 2a is the same as Category 1, but with a large region of near-zero intensity between $L = 5$ and $L \approx 7$ $R_S$, from the lowest energy up to about 100 keV/e. Category 3a is further decayed, with the significant difference being the full decay of all $W^+$ energies for $L < 7$ $R_S$. Category 4 is the most decayed, encompassing any profiles with full dropout of all $H^+$ and $W^+$ energies for $L < 7$ $R_S$ or more.

Going from an "a" to a "b" suffix on a category name denotes the inclusion of a recent injection signature that is superposed on the formerly decayed $L < 7$ $R_S$ region. These injections counter the charge exchange depletion. An injection signature looks like a group of sharp, bright, nearly vertical lines going from high intensity at 3 keV/e smoothly to lower intensity at around 30 keV/e. Examples of injection signatures, as well as profiles from all 6 categories, are shown in Figure 4.

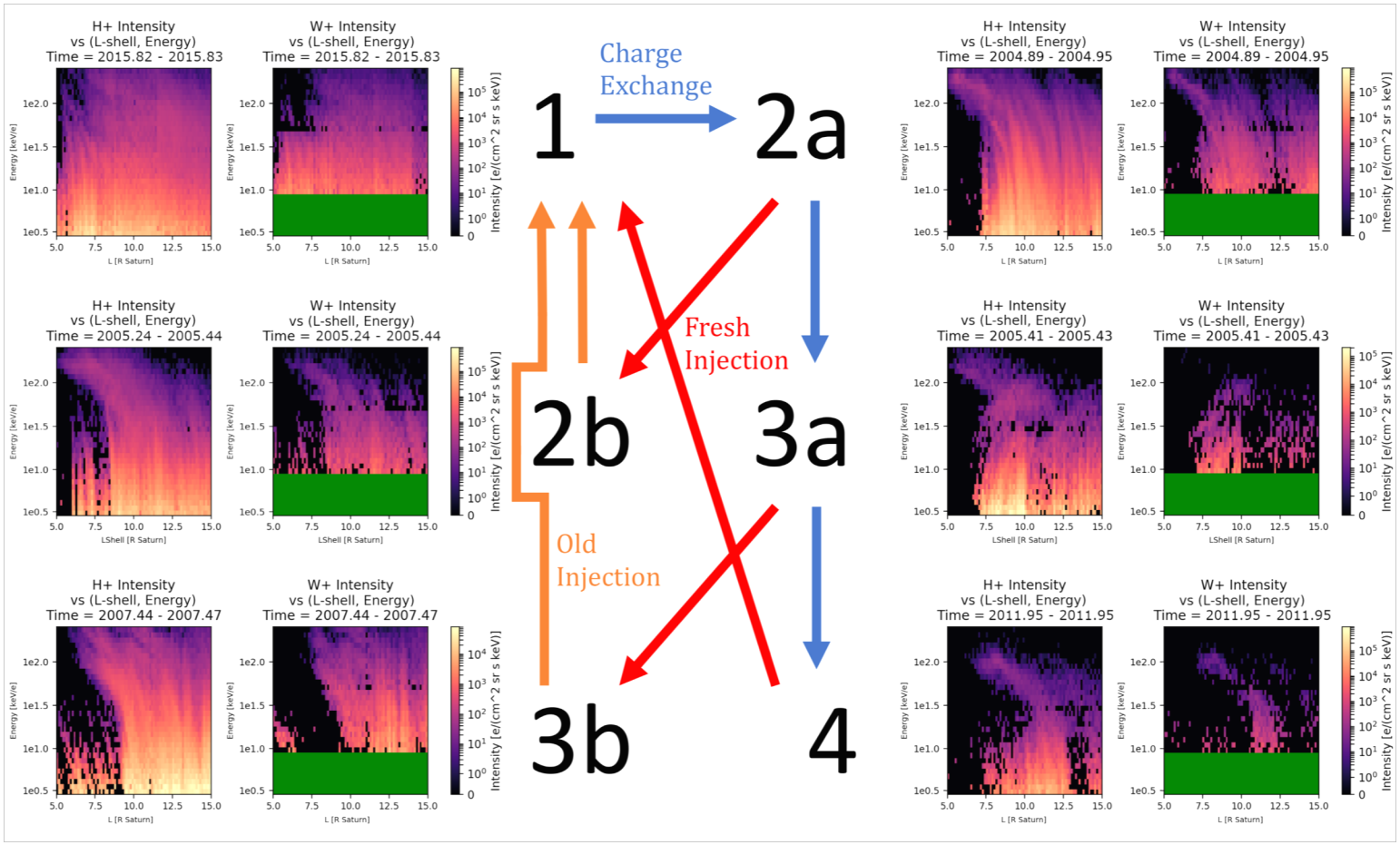
H+ Intensity
vs (L-shell, Energy)
Time = 2015.82 - 2015.83
W+ Intensity
vs (L-shell, Energy)
Time = 2015.82 - 2015.83
H+ Intensity
vs (L-shell, Energy)
Time = 2004.89 - 2004.95
W+ Intensity
vs (L-shell, Energy)
Time = 2004.89 - 2004.95
H+ Intensity
vs (L-shell, Energy)
Time = 2005.24 - 2005.44
W+ Intensity
vs (L-shell, Energy)
Time = 2005.24 - 2005.44
H+ Intensity
vs (L-shell, Energy)
Time = 2005.41 - 2005.43
W+ Intensity
vs (L-shell, Energy)
Time = 2005.41 - 2005.43
H+ Intensity
vs (L-shell, Energy)
Time = 2007.44 - 2007.47
W+ Intensity
vs (L-shell, Energy)
Time = 2007.44 - 2007.47
H+ Intensity
vs (L-shell, Energy)
Time = 2011.95 - 2011.95
W+ Intensity
vs (L-shell, Energy)
Time = 2011.95 - 2011.95
Energy [kev/e]
L [R Saturn]
LShell [R Saturn]
Intensity [e/(cm^2 sr s keV)]
Charge
Exchange
1
2a
2b
3a
3b
4
Fresh
Injection
Old
Injection

*Figure 4: Separation of half-orbit profiles into 6 categories: 1, 2a, 2b, 3a, 3b, and 4. These categories are distinguished by qualitative differences in the shapes of the $H^+$ and $W^+$ intensities and are explained in Sec. 3.1. Once these categories are made, we hypothesize how a combination of charge exchange and injection processes might move an intensity profile through them, as shown by the color-coded arrows.*

After defining these categories phenomenologically based on real differences in the observed data, we noticed that their temporal spatial/energy evolution may be consistent with charge exchange and injection processes. Therefore, we hypothesize that charge exchange is a dominant mechanism in organizing the suprathermal ion data, especially the protons, as measured by CHEMS. The color-coded arrows in Figure 4 illustrate the paths that injections and charge-exchange-like process may take. Blue arrows represent the loss process that we hypothesize may be charge exchange. The progressive decay of low $L$, low to high E regions moves a profile from 1, to 2a, to 3a, and finally to 4. At any point, a fresh injection could occur, represented by the red arrows. This will move a 2a to a 2b, or a 3a to a 3b. As these injections age (orange arrows), they will fill up intensity profiles smoothly from low to high energy, bringing them back to category 1. Note that the transition from category 4 to 1 is not given a "b" step. This is because category 4 is already very sparsely populated: few intensity profiles decay long enough without a new injection to deplete the high energy $H^+$. However, when a category 4 profile experiences an injection, we expect that it would mirror its 2a and 3a counterparts, quickly moving from a fresh injection signature to a full category 1 profile.

While many of Cassini's orbits have a closest approach closer than $L = 5$ $R_S$, some do not. These orbits either do not enter the 5-15 $R_S$ region, or they reach closest approach somewhere within that range. In the former case, the inbound and outbound half-orbits are both empty of useful data for this study. In the latter, they include data only from $L = 15$ down to some $L_0 > 5$ $R_S$. Since the low $L$ region is most active for charge exchange and injection processes, these stunted half-orbits are often also less than helpful. The proliferation of such orbits inhibits the direct comparison of multiple consecutive half-orbit profiles that would allow for a more straightforward observation of the progression through categories. Thus, we neglect orbits that do not reach down to 5 $R_S$ and only compare inbound and outbound orbits that do reach within that distance.

## 2.2 Physical Model

To quantitatively test our charge exchange hypothesis (illustrated by the categories in Figure 4), we develop a physical model of charge exchange that takes a half-orbit intensity profile as an initial condition. Charge exchange obeys the differential equation

$$\frac{\partial f}{\partial t} = -f v n \sigma \qquad (1)$$

where $f$ is the phase space density in $s^3\ kg^{-3}\ m^{-6}$, $v$ is the velocity of the ions in m/s, $n$ is the density of the neutral gas in $m^{-3}$, and $\sigma$ is the charge exchange cross section of the ion on the neutral gas in $m^2$. For this study, the ions are $H^+$ and $W^+$. We assume that $v = \sqrt{\frac{2E}{m}}$ in the nonrelativistic limit $v \ll c$, which is valid for suprathermal ions spanning 3-220 keV/e .

We assume that the neutral torus is dominated by $H_2O$ near Enceladus and by O otherwise (Cassidy et al. 2010; Fleshman et al. 2012). We approximate the densities through

exponential radial density distributions that in their nominal setting approximate the Cassidy et al. 2010 densities but can be easily changed in amplitude and shape to optimize our model (as discussed below and in Fig. 10B). The nominal distribution is shown in Figure 5. With this information, as well as charge exchange cross sections reported by Lindsay et al. (2005) and Gobet et al. (2001), we can evaluate the time derivative of phase space density due to charge exchange at every point "E, *L*" in a half-orbit intensity profile. Including a term for radial diffusion (see section 5.2) and using an explicit Runge-Kutta method, we approximate a solution for phase space density at a set of time values. The derivative is smooth everywhere and generally small compared to the phase space density over the timesteps used, so we can be confident that the approximate solution is more than sufficiently close to accurate without requiring extravagant computing power. With this model, then, we can predict how charge exchange will decay an intensity profile. By evaluating the solution at different time values and locations (Fig. 6), we can see how this decay will look after arbitrary times, including at the actually observed locations and times (Fig. 7).

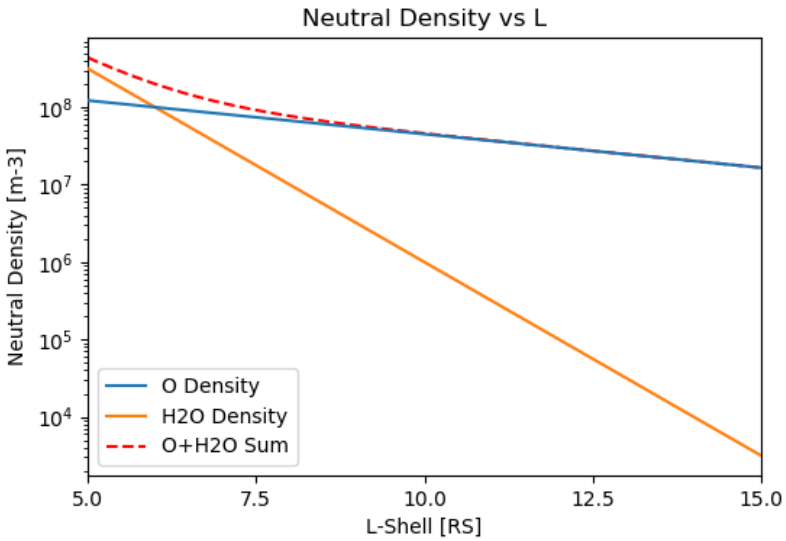


*Figure 5: Neutral density radial distribution that we use for the charge exchange model. The blue line represents neutral oxygen, and the orange line represents neutral water. The dotted red line is their sum, shown to give a sense of how much each gas contributes to the total neutral density.*

To see if our charge exchange model accurately predicts how the intensity profiles evolve, we find 40 pairs of consecutive half-orbits that 1) fully cross the $L = 5$ to 15 $R_S$ region twice within a 2.5 day period and 2) have valid measurements for more than 95% of the E by *L* region. This limits us to orbits whose closest approach is just barely less than 5 $R_S$, so the inbound and outbound traversals of the region of interest are as temporally close as possible. We refer to each traversal as the "in frame" portion of the half-orbit. For each of these 40 inbound and outbound half-orbit pairs, we use the first intensity profile as an initial condition for the charge exchange model, and then compare the results to the second profile.

To do this, we initially assumed that ion drift paths around Saturn were circles, i.e. symmetric in local time. To first order approximation, this worked. However, in order to

successfully compare predicted and measured profiles sourced from opposite sides of Saturn, some fine tuning was needed. Thomsen et al. (2012) report on local time asymmetries caused by a global noon-to-midnight electric field, pushing ion drift paths into an ellipse. To account for this, we keep track of "$L_N$" for particles, the L-shell that their drift paths reach at local midnight. For the remainder of this study, "constant $L$" refers to these elliptical trajectories, which are in reality constant $L_N$. This provides sufficient accuracy for our model comparison. Further discussion on our correction for this is provided in Appendix A.

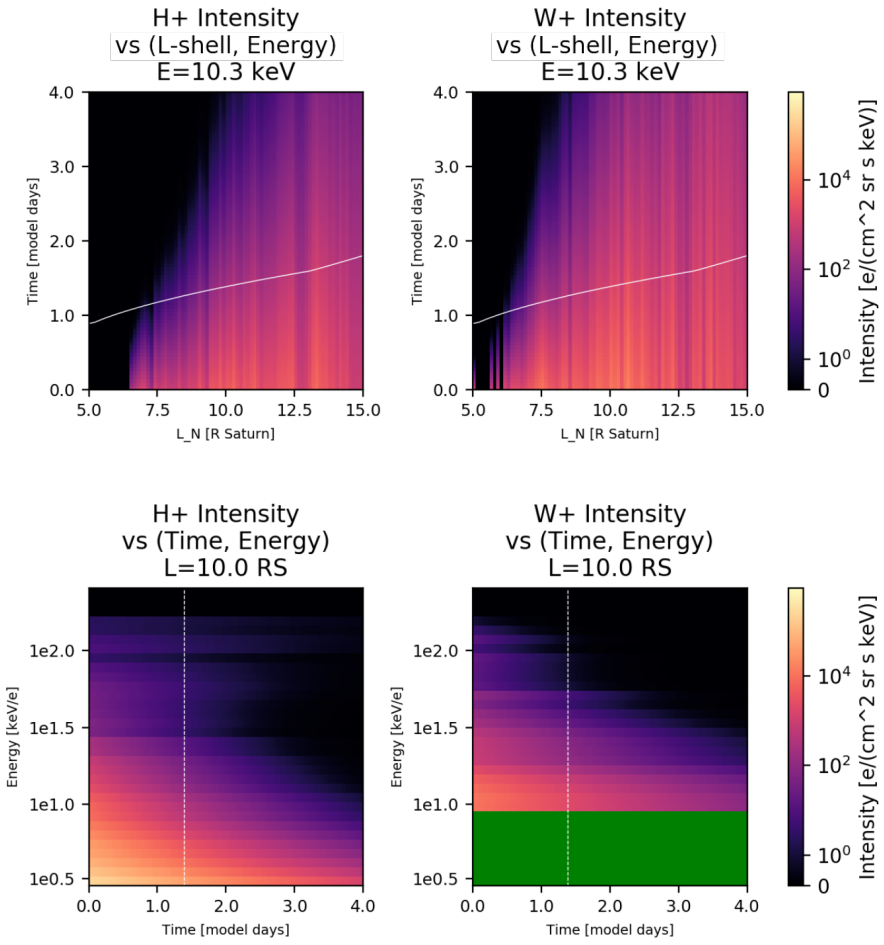


*Figure 6: Slices of the modeled "L-shell, energy, time" space at constant E=10.3 keV/e (upper panels) and constant L=10 $R_S$ (lower panels). Time is reported in "model days" which is equivalent to "days since initial condition." The solid white lines in the upper panels show Cassini's outbound trajectory through L and time. The vertical dashed white lines in the lower panels show the time at which Cassini crossed the L=10 $R_S$ slice shown.*

In order to predict the intensity profile that CHEMS will measure on its outbound trajectory, we divide the 5-15 $R_S$ L-shell range into 80 segments, calculate the time at which Cassini crossed each one moving away from Saturn, and evaluate the model at those 80 discrete time steps. In essence, we take into account Cassini's path through "L-shell, energy, time" space. This can be visualized by looking at slices of constant energy and constant $L$, as shown in Figure 6. We assume that the initial condition intensity profile is true all together for a single instant, and call that $t = 0$ for the model. By defining this

instant to be the mean of when Cassini entered the region of interest at $L = 15$ $R_S$ and when it exited at $L = 5$ $R_S$, we can reliably map model time to universal time, as shown in Figure 7.

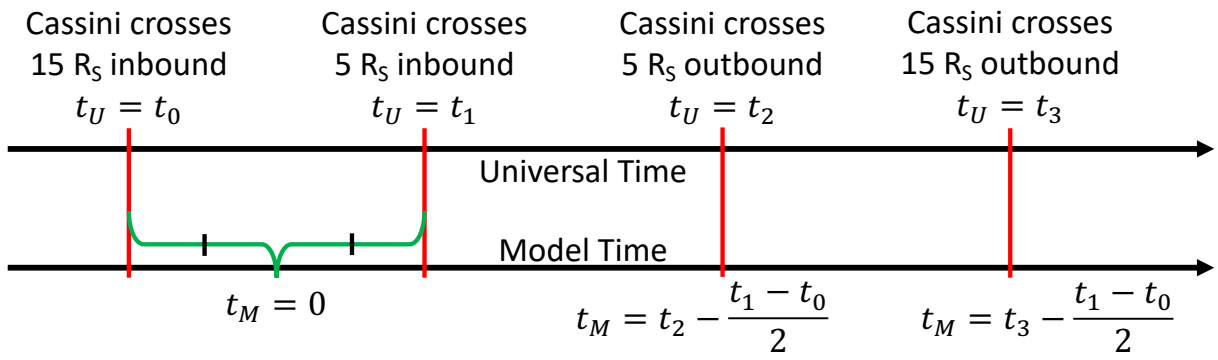


*Figure 7: Timelines for universal time and model time placed side-by-side to show how the initial condition is assumed to happen instantaneously, but the compared portion takes into account Cassini's trajectory through model space.*

For each comparison, we assign an error score to every E, $L$ pixel of the predicted profile. The score $s = \left(\text{symlog}(j_{predicted}) - \text{symlog}(j_{measured})\right)^2$. The symlog function is a piecewise function that is linear for inputs from 0 to 1, and logarithmic for inputs greater than 1. It is defined specifically as:

$$\text{symlog}_m(x) = \begin{cases} 0 < x < 1: & \dfrac{x}{\ln(m) + 1} \\ x \geq 1: & \dfrac{\ln(x) + 1}{\ln(m) + 1} \end{cases}$$

for expected maximum input $m$, which will be mapped to 1. We use $m = 9 \times 10^5$. This function is designed such that the two piecewise sections have equal values and first derivatives at the break point. We plot this error score on an energy versus L-shell grid along with the predicted and compared intensity profiles, and we sum up the total error from all the pixels and assign that to the comparison as a whole. With 80 bins in $L$ and 32 bins in energy (due to instrument sensitivity, see Vandegriff et al. 2018), and a maximum error per pixel of unity, the maximum possible error score for a comparison is $2.56 \times 10^3$ for $H^+$ and $1.92 \times 10^3$ for $W^+$. Error scores for visually "good" predictions tend to be less than 100. These error plots and scores can be seen in Figure 9 and will be discussed further in section 3.

## 3. Results

The losses in the proton plots are well replicated by the charge exchange model, suggesting that this is the dominant loss process for this species between 5 and 15 $R_S$. One example comparison is shown in Figure 8. The predicted and measured intensity profiles

are very similar in form, and share some notable features. They both have decay in the low $L$ region along similar lines, as well as the high energy region. They both have similar looking low intensity features from $L$ = 8 to 10 $R_S$ at 100 keV/e. The predicted profile looks like a "smoothed out" image of the measured profile.

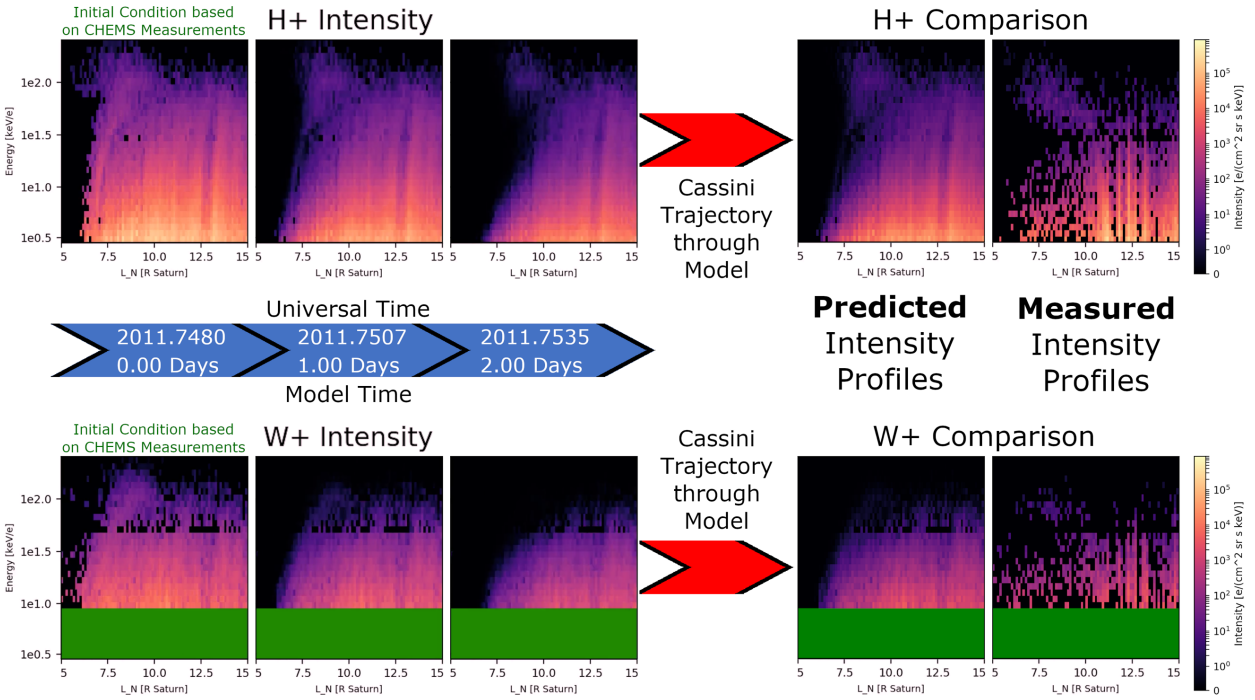


*Figure 8: Schematic showing the modeling and comparison process at a high level for one example pair of inbound and outbound half-orbits. The leftmost panels on the top and the bottom show actual CHEMS measurements, which are used as initial conditions for the charge exchange model. The second and third panels from the left show snapshots of the model taken 1 day and 2 days after initiation. The blue arrow between them shows the mapped universal and model times. The second panels from the right show the predicted intensity profiles, taking into account Cassini's trajectory through model space. The rightmost panels are the actual measurements of the subsequent outbound half-orbit.*

CHEMS measures intensity by counting the number of particles per unit time that fulfill coincidence requirements (Vandegriff et al., 2018). The speckled pattern is due to low-count statistics resulting from short averaging time. When summed over many timesteps, the number of counts increases and thus the expected variance decreases, so the data is smoothed out. For half-orbits like these, though, chosen specifically for the high speed at which Cassini traverses the region of interest, smooth real intensity may produce speckled data.

Further examples of such comparisons, along with their associated error plots, are shown in Figure 9. Compared to the amount of variation between intensity profiles of different orbits, the charge exchange model's predictions very closely approximate the measured data. We are able to reproduce all categories of observations that do not require additional injections during the time evolution, suggesting that we are able to reproduce the full time dependence, which is more difficult to fit with a model than a snapshot in time. Accuracy of prediction using a physical model implies that the physical processes included in the model are the dominant processes on the timescale used. Therefore, these results

evidence the role of charge exchange as the dominant loss process for 3-220 keV protons between $L$ = 5 and 15 $R_S$.

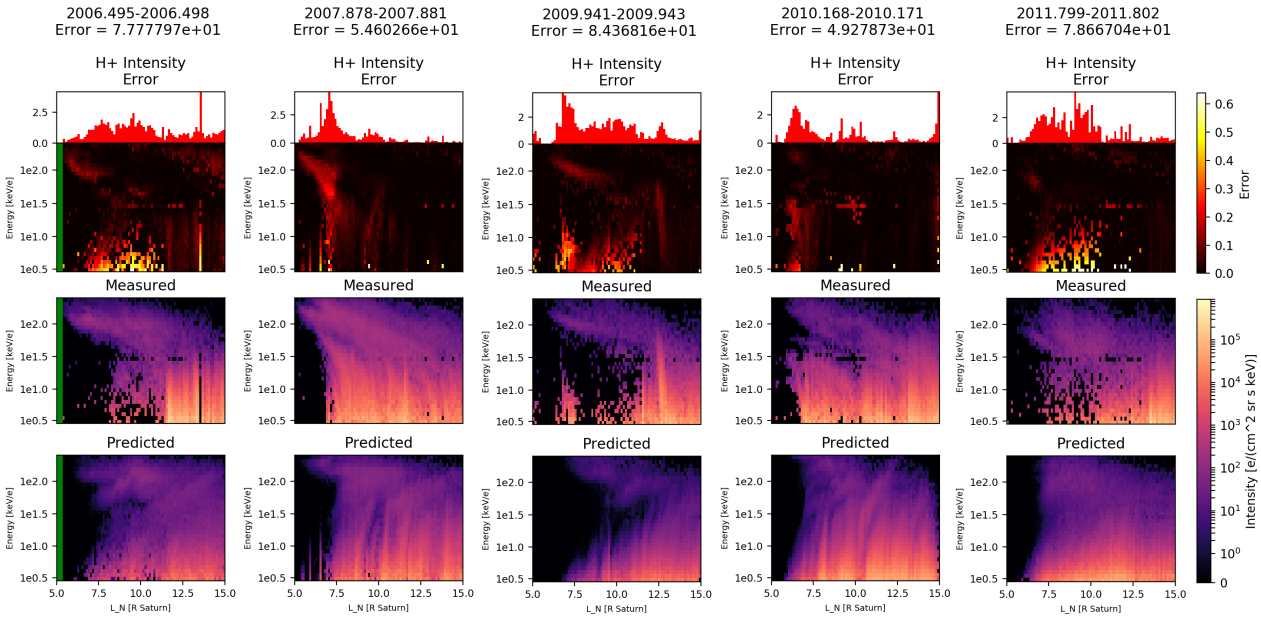


*Figure 9: Comparisons between measured $H^+$ intensity profiles (second from last row) and their associated predicted profiles (last row) for 5 outbound passes. The universal time and total error score are provided at the top of each comparison, as well as a bar graph dividing error by L-shell and a color plot dividing error further by energy. The color scales for intensity and error are shown at the far right.*

As well as displaying those areas where the model breaks down, the error plots are very effective at picking out and portraying fresh injection signatures. Injections yield large errors because they are not captured by our model that only includes steady charge exchange losses. In the 3rd comparison in Figure 9, note how the measured intensity profile has an injection signature at $L$ = 7.5 $R_S$. This same injection signature can be seen in the associated error plot, with the expected background intensity effectively removed. In cases like this, where an injection occurs between Cassini's inbound and outbound trajectories, the error plot for the comparison could be used to characterize its signature.

In order to achieve these results, we allow a scale factor for neutral density to be a free model parameter. The shape of the radial distribution given in Figure 5 remains the same for every half-orbit pair, but we allow it to be multiplied by a constant. The constant is first chosen by an algorithm to minimize error score, and then fine-tuned by hand to match higher level features. A scatterplot of scale factor versus universal time is shown in Figure 10A. As can be seen in Figure 10B, the majority of scale factors that we use are not out of the ordinary compared to other studies' estimates of Saturn's neutral torus density (Cassidy et al., 2010; Dialynas et al., 2013; Melin et al., 2009; Richardson et al., 1998; Smith et al., 2010). The observed rate of charge exchange lends credence to the higher end of the density distribution spectrum. The apparent time variability is likely an artifact of model simplifications explained in Sec. 4.4.

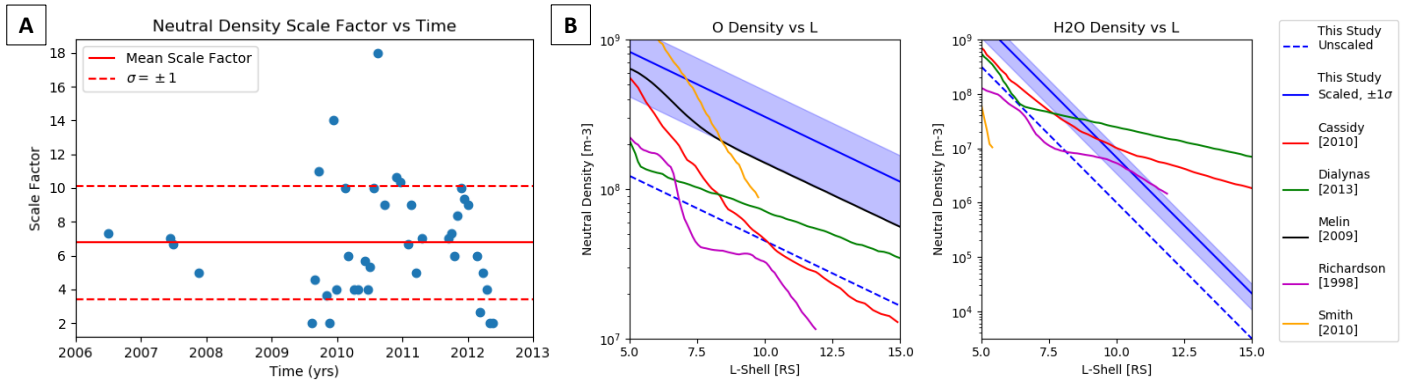


*Figure 10: A) Neutral density scale factor used in our model versus universal time. For each half-orbit pair we choose a scale factor for neutral density in order to best match the prediction to the measured data. The solid red line is their mean, and the dashed red lines show one standard deviation above and below the mean. B) Neutral density radial distributions used by this study and others. The dashed blue lines are the data from Figure 5, corresponding to scale factor 1. The solid blue lines correspond to the mean scale factor (~7) and the blue shaded regions show one standard deviation of scale factor above and below the mean.*

The model does not replicate losses in the water group ions (Fig. 11) as well as it does in the protons (Fig. 9). It is most accurate in the lower energies, from 10 to 50 keV/e and in the higher L-shells, from 7.5 to 15 $R_S$. It consistently underestimates intensities in the high energy, low *L* region. The measured data is often nonzero but dim in this region, while the model predicts uniformly zero intensity. The model's error for the low energy, low *L* region does not trend strongly in either direction. When compared to the variability between different pairs of half-orbits, the model still does a good job, especially in its most accurate region. This suggests that charge exchange is the dominant loss process for 10 to 50 keV $W^+$ ions from $L = 7.5$ to 15 $R_S$, but that other processes may play a major role in lower *L* or higher E. Examples of water group ion comparisons can be found in Figure 11, as well as the one displayed in the bottom half of Figure 8.

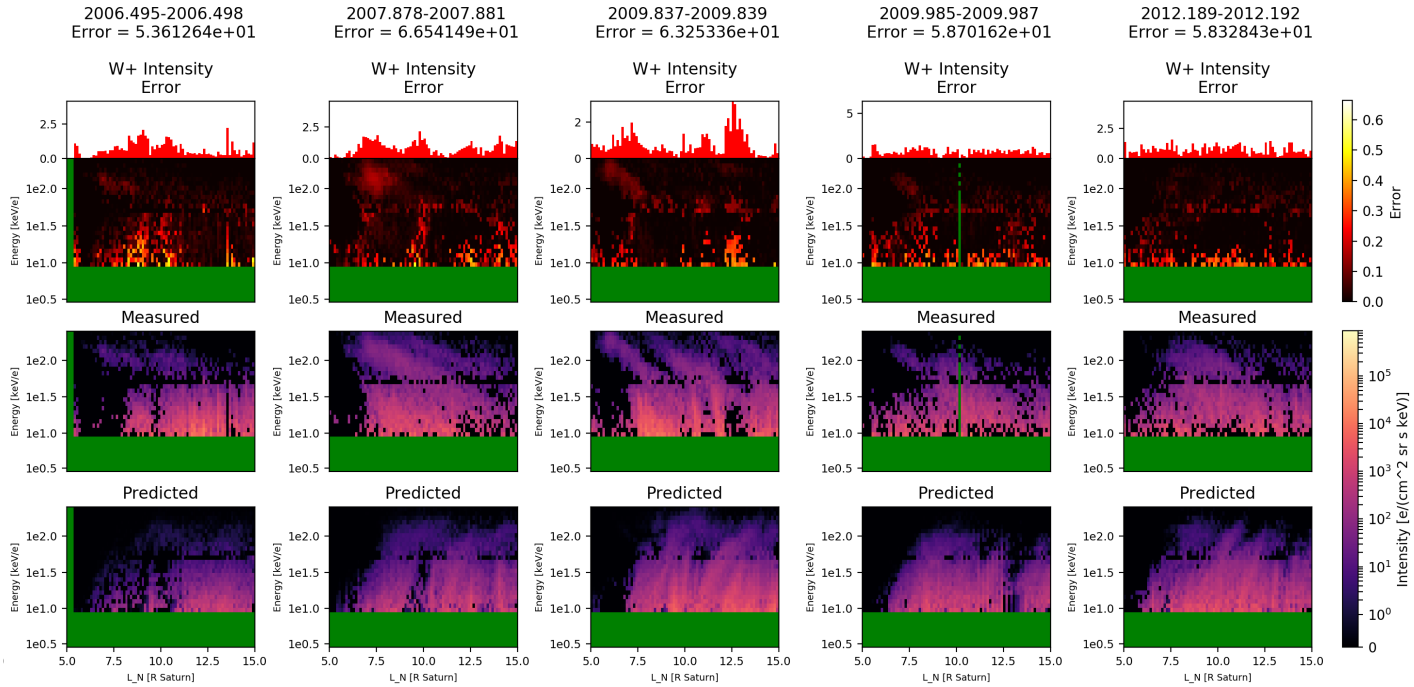


*Figure 11: Same format as Fig. 9 but showing $W^+$ ions.*

The error score for the model is derived such that it can only be used to draw meaningful conclusions about model performance within a single species, rather than between species. A true measure of model performance between species would need to take into account the difference in "intra-species variation" between $H^+$ and $W^+$. For example, if all of the $W^+$ profiles were nearly identical, while each $H^+$ profile was wildly different from the last, a model with reasonably constant expected performance would show significantly less error in the former than the latter. To a less extreme extent, this is what we are seeing: model error scores are lower for water group ions, even though model performance is visibly better for protons.

As can be seen in Figure 11, the low energy regions of $W^+$ predictions tend to have only scattered error, not trending strongly toward overestimation or underestimation. This may be attributed to a few different limitations discussed further in section 5, but likely does not invalidate the conclusion that charge exchange is the dominant loss process involved. On the other hand, the consistent underestimation of the model in the high energy (~60-220 keV/e) and low $L$ ($\lesssim 9$ $R_S$) region points to the possibility of a source process for water group ions in this vicinity. The only source process yet considered in this study is injections, and these have very different signature characteristics from the $W^+$ errors shown. In the top left of every error plot in Figure 11, one can see a consistent but dim red mass that looks very different from the aforementioned injection signature error in Figure 9. One likely hypothesis for this source is the presence of $W^{2+}$ charge exchanging into $W^+$, which will be further discussed in section 4.3.

## 4. Discussion: Interpretations

### 4.1 Ambiguity between charge exchange and dispersion

Our model's ability to accurately predict how an intensity profile will evolve in time reveals that charge exchange is the dominant loss process in Saturn's magnetosphere between 5 and 15 $R_S$ for 3-220 keV protons and 10-50 keV $W^+$ ions (see results in Figures 9 and 11). At first glance, distributions falling in categories 2-4 resemble old injection signatures, dispersed in local time according to energy and location. This objection merits a discussion. As mentioned in section 2.1, the time constraint on the total elapse between half-orbits requires that the first be inbound and the second be outbound. We require this time constraint because it falls within the theoretically derived timescale for charge exchange (see section 4.2) and because it is short enough that fresh injections between measurements are sparse. Because of this, it is unavoidable that all of the inbound segments be initial conditions which are then modeled and compared to all of the outbound segments.

Studies of injection signatures in Saturn's magnetosphere (Mauk et al., 2005; Paranicas et al., 2010) show that they begin as radial (constant local time) lines, but as they age, azimuthal diffusion spreads them out according to energy. High energy $H^+$ and $W^+$ ions drift faster than their low energy counterparts. Saturn's magnetosphere does not enforce rigid corotation but causes particles with smaller radial distance to corotate faster than those farther out. The energy and location dependence of the drift speed as well as the spacecraft orbit determine if the high or low energy particles of a given charge state are detected first. Older injection signatures appear to curve in an energy versus $L$ plot, because Cassini will experience an energy gradient as it moves through the dispersed injection while also moving through $L$. With a realistic corotation profile included, the curvature of the inbound portion should usually show the highest ion intensities at large distances (Mauk et al., 2005). However, we commonly observe the opposite for protons: the highest energies are found at small radial distances, regardless of whether Cassini is moving inbound or outbound. $W^+$ ions sometimes show the opposite behavior compared to protons. Such a difference is inconsistent with these structures being a result of injections, which organize by charge. It is however consistent with charge exchange, which is more efficient for $W^+$ and removes high energies at small distances.

### 4.2 Charge exchange particle lifetimes

From the charge exchange equation (1), we can define a characteristic time constant

$$\tau_{CE} = \frac{1}{nv\sigma} \qquad (2)$$

that corresponds to the mean lifetime of an ion before it becomes an ENA. Using the mean of the scale factors for the different neutral density models shown in Fig. 10 and taking into account both O and $H_2O$ neutrals, particle lifetimes for $H^+$ and $W^+$ are calculated in Figure 12. For the region and particle energies of this study, lifetimes vary from $10^3$ s ≈ 17 min to $10^6$ s ≈ 12 days.

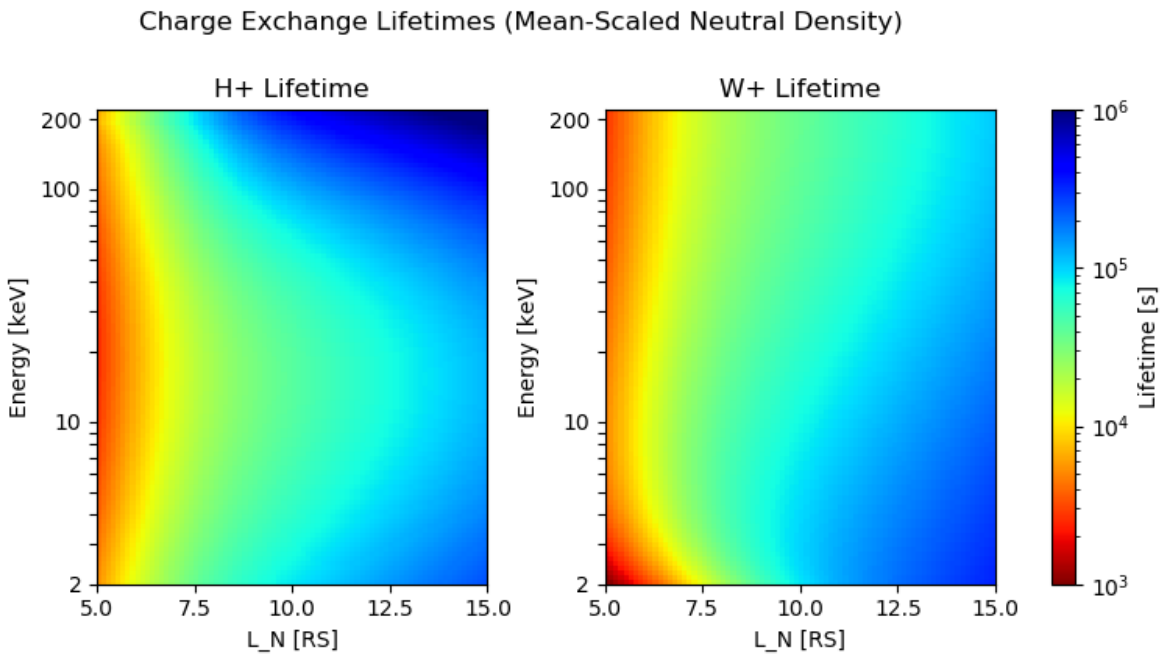


*Figure 12: Plot of particle lifetime due to charge exchange versus energy and L-shell according to Eq. (2). Lifetime is calculated using the mean scale factor for neutral density, taking into account both neutral O and $H_2O$ and their respective cross sections.*

The near alignment of these lifetimes to the timescale of Cassini's consecutive half-orbits motivates our insistence on the restriction given in section 4.1. In addition, these plots of ion lifetime provide a "characteristic shape" of profiles being depleted by charge exchange. They further validate the progression of profile categories given by Figure 4. First the low L-shell, low to middle energy $H^+$ and $W^+$ are removed, then the high energy $H^+$, then continually higher *L* values until a fresh injection occurs. Finally, the low lifetime of high energy, low L-shell $W^+$ ions shows that the model's consistent underestimation of $W^+$ intensity in that region is due to some process other than charge exchange, rather than an error accrued from approximating the differential equation or other parameters.

## 4.3 Possible $W^+$ source process

As illustrated in Fig. 11, the charge exchange model consistently underestimates the intensity of $W^+$ in the high energy, low *L* region. All cited studies agree that the low L-shells have the highest neutral densities between 5 and 15 $R_S$ (Cassidy et al., 2010; Dialynas et al., 2013; Melin et al., 2009; Richardson et al., 1998; Smith et al., 2010). High energies correspond with high velocities, regardless of species. Together, these factors suggest that charge exchange lifetimes will tend to decrease towards the low *L*, high energy region for all ions. The magnitude of this tendency is dependent on an ion's charge exchange cross sections. In any case, the model's inaccuracy is localized in a region characterized by strong charge exchange.

This observation, along with the presence of $W^{2+}$ in Saturn's magnetosphere, suggests that charge exchange may act as both a source and loss process for $W^+$ ions. The $W^+$ ions

are charge exchanging into W ENAs, while the $W^{2+}$ ions are charge exchanging into $W^{+}$. This is not accounted for in the present model, which explains its consistent underestimation. $W^{2+}$ ions are less abundant than $W^{+}$ by approximately 1.5 orders of magnitude (DiFabio, 2012) which further explains the dimly persistent intensity as well as the lack of noticeable error in regions of already intense $W^{+}$. In the high energy, low $L$ region, charge exchange quickly depletes the $W^{+}$ ions, as per the short lifetimes shown in Figure 12. Simultaneously, charge exchange is everywhere turning $W^{2+}$ ions into $W^{+}$ ions. This occurs more slowly than the $W^{+}$ loss, since charge exchange rate is proportional to ion intensity. Because of this, the $W^{+}$ gain is slow compared to its loss, and is therefore unnoticeable for the majority of this study's region of interest. However, where charge exchange has already depleted $W^{+}$ to an intensity comparable to $W^{2+}$, this gain will show up as an underestimation of the model.

This hypothesis has yet to be explored from a modeling approach. Such an exploration would begin by pulling multiply-charged water group ion counts from the CHEMS data and confirming that $W^{2+}$ can be found between $L = 5$ and 7 $R_S$ at energies between 60 and 200 keV/e. It would continue by finding the charge exchange cross sections of $W^{2+}$ ions at those energies and determining if particle lifetimes are low enough to fit the observed data. Finally, $W^{2+}$ ion intensity profiles could be included alongside $H^{+}$ and $W^{+}$ in the charge exchange model, in order that $W^{2+}$ losses could be directly presented as $W^{+}$ gains.

### 4.4 Neutral density results

As discussed in section 3, we allow neutral density scale factor to be a free parameter in the charge exchange model, using a fitting algorithm to minimize error scores and then fine tuning by hand to match intensity profile features. These scale factors are plotted in Figure 10A. The mean scale factor is ~7, and the standard deviation is ~3.

One assumption made in the model is that $f$, $n$, $v$, and $\sigma$ from the charge exchange differential equation (1) are independent of latitude along a particle's trajectory and thus can be expressed purely as explicit functions of L-shell, energy, and time. This is true for $f$ and approximately true for v and $\sigma$. These are dependent only on energy, which remains nearly constant (Sec. 5.2).

Neutral density, however, changes with latitude in addition to $L$, so a particle's bounce motion brings it through different neutral densities. To account for this, we can define:

$$n = \frac{1}{\tau_b} \oint n(\vec{r}) |\vec{v}| \, dt$$

as the time-averaged neutral density we expect a particle to experience, for bounce period $\tau_b$. In principle one can use numerical integration to calculate this time-averaged density for any assumed neutral distribution and arbitrary values of the measured equatorial pitch angle. Particles with equatorial pitch angles around 90° have low mirror latitudes, and thus spend more time in the dense portions of the neutral torus resulting in faster charge exchange losses, and vice versa for field pitch angles near 0°. Density usually decreases with latitude, meaning that the average density is lower than the peak equatorial density.

However, there are variations of up to an order of magnitude in the published equatorial densities, see Figure 10B, even though equatorial values are relatively well constrained. Latitudinal profiles on the other hand are even less constrained, which is why often only column densities are provided instead of $n(\vec{r})$. What we do find qualitatively is that the density we determined by optimizing our models is a lower limit for the equatorial density. The equatorial densities need to be increased from our nominal value by more than the factor of ~7 we find for the average scale factor. Such large values can be explained by the large uncertainty of what we picked as a nominal value, also included in Figure 10B.

Measurements at different orbits typically measure different pitch angles, naturally resulting in different average densities. This is likely the reason for the required variation of the scale factor over time. On top of these variations resulting from observation bias may be true variations of the density. Repeated observations of Enceladus' plumes, which supply most of the neutral gas, show that their density and strength can vary by up to an order of magnitude on short timescales (Teolis et al., 2017). Smith at al. (2010) use a particle simulation for these plumes to show that a factor of 4 increase in plume density and strength brings about a factor of ~3 increase in density for all water group neutral species. However, we currently cannot distinguish variations from bias and from true time dependence.

## 5. Discussion: Limitations

### 5.1 Injections

Because the injection process is not as straightforward to quantify as charge exchange, and because an injection's size and time duration appear stochastic given current data, we do not attempt to account for them within the physical model for the lack of accurate constraints. This limits our ability to accurately predict the evolution of intensity profiles at small distances and low energies. However, injections have distinct signatures in the data so that their respective data-model discrepancies can be easily identified.

### 5.2 Radial Diffusion

Radial diffusion is the process by which fluctuations in Saturn's magnetosphere cause ions to spread out radially while conserving the first adiabatic invariant. The first adiabatic invariant $\mu = \frac{E \sin^2 \alpha}{B}$ is associated with particle gyromotion. The second is associated with bounce motion, and the third with drift motion. Each adiabatic invariant remains constant under continuous changes in the electromagnetic field, as long as those changes happen slowly over the course of their associated motion. Field fluctuations on timescales longer than the bounce motion bring about radial diffusion (Lejosne and Kollmann, 2020). Because the magnetic field drops like $L^{-3}$, the first adiabatic invariant at constant pitch angle $\mu \propto EL^3$.

We include radial diffusion by adding the charge exchange term from equation (1) to the diffusion term:

$$\frac{\partial f(\mu, K, L)}{\partial t} = L^2 \frac{\partial}{\partial L}\left(\frac{D_{LL}}{L^2}\frac{\partial f}{\partial L}\right)$$

The partial derivatives with respect to L-shell imply that the first and second adiabatic invariants, $\mu$ and $K$, are held constant. At constant $\mu$ and pitch angle, $E \propto L^{-3}$. We approximate $\frac{\partial f}{\partial L}$ at constant $\mu$ as $\frac{\partial f}{\partial L}$ at constant energy. Effectively, this causes the model to ignore "adiabatic heating," the process by which radial diffusion along lines of constant $\mu$ causes ions to increase in energy as they decrease in L-shell, and vice versa. This simplification is not critical because radial diffusion is slow in comparison with charge exchange. When we compare our modeled intensity profiles with and without this approximation of radial diffusion, the differences are hardly noticeable.

## 6. Summary

In this study, we have developed a physical charge exchange model whose predictions we compare to measured data in an effort to better understand the ion loss processes in Saturn's magnetosphere. Below is a summary of our results and discussion points:

1) Orbital intensity profiles of suprathermal proton and water group ions follow distinct qualitative categories, from which we hypothesize charge exchange as the driving loss process.
2) The measured losses between inbound and outbound passes shown by the $H^+$ intensity profiles are well replicated by the charge exchange model, suggesting that charge exchange is the dominant loss process and driver of the observed variability for 3-220 keV protons between 5 and 15 $R_S$.
3) By allowing a scale factor for neutral torus density to be a free parameter within the model, we show that the observed rate of charge exchange lends credence to those studies from Figure 10B with higher end neutral density estimates (Melin et al., 2009; Smith et al., 2010).
4) The measured losses between inbound and outbound orbit pairs shown by $W^+$ intensity profiles are well replicated by the model in the low energy (<50 keV/e) and middle-to-high L-shell (>7.5 $R_S$) regions. The model's error in the high energy, high L-shell region tends strongly toward underestimation, suggesting that there may be a gain process for water group ions there.
5) We propose that charge exchange turning $W^{2+}$ into $W^+$ is a feasible gain process to explain the model's localized underestimation in water group intensity profiles. Further exploration would be needed to see if the intensity and cross sections of multiply charged water group ions could reproduce the observed gains.

## Appendix A: Local time asymmetry L-shell shift due to electric field

As mentioned in section 2.2, the presence of a noon-to-midnight electric field (Thomsen et al., 2012) causes ions to drift around Saturn in an ellipse. This characteristic was originally detected based on the difference in L-shell of drifting particles between local noon and local midnight. Thus, an elliptical drift path is characterized by its "$L_D - L_N$" factor, for L-shell at midnight $L_N$ and L-shell at noon $L_D$. We account for this in the model by converting $L$ into $L_N$ based on local time. The ability to do this is mathematically equivalent to drawing contours of constant $L_N$, which are by definition the elliptical drift paths of ions when the electric field is taken into account. One such contour/path is drawn in blue in Figure 13.

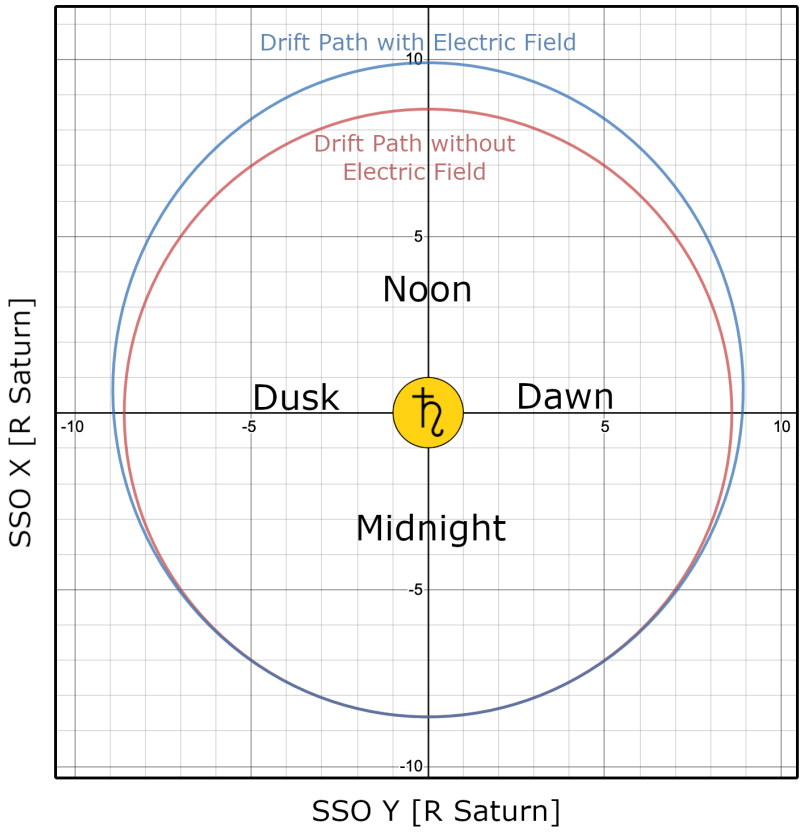


*Figure 13: Drift paths for ions moving around Saturn with and without a noon-to-midnight electric field.*

To draw such an ellipse, four known points (or pieces of distinct information) are required. For a given $L_N$, the first point is trivially $L = L_N$ at local midnight. The second point is $L = L_N + (L_D - L_N) = L_D$ at local noon, using the observed "$L_D - L_N$ versus $L_N$" curves reported by Thomsen et al. (2012). The third and fourth pieces of information require assumptions on our part. We first assume that the drift path will be symmetrical across the noon-to-midnight line. This is a safe assumption, because the electric field causing the elliptical drift path shows this symmetry, and no other significant local time asymmetries in drift path are taken into account. Our second assumption and final piece of information is that the curvature of the ellipse at local midnight is equal to the curvature of the circle, or $\kappa_N = L_N^{-1}$. We choose this because it minimizes the difference

between $L$ and $L_N$ everywhere while requiring that $L \geq L_N$, with the only point of equivalence at local midnight. This can be seen in Figure 13 by the red and blue paths appearing nearly identical on the nightside, but monotonically diverging toward noon in either direction.

Instead of plotting and evaluating derivatives along lines of constant $L$, we now can do so along lines of constant $L_N$, which are the actual particle trajectories. We call this transformation the "L-shift," because its results look like shifting the middle section of a Y versus $L$ plot to the left. To test if this shift feasibly matches the CHEMS data, we apply it to a plot of the mission-averaged $H^+$ intensities versus L-shell, divided into local day and night measurements. This is shown in Figure 14.

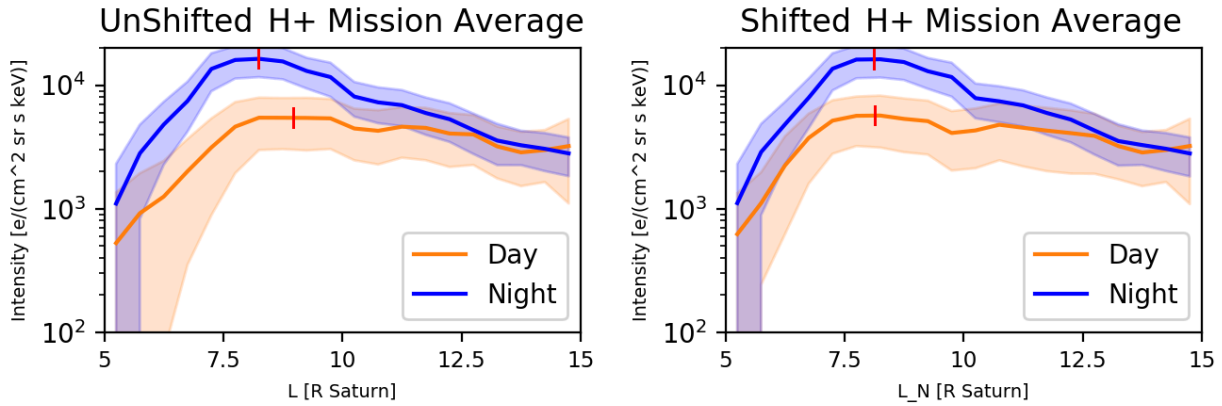


*Figure 14: The comparison between mission-averaged $H^+$ intensities versus L-shell, divided into local day and night components, for the unshifted and shifted datasets. The orange lines correspond to day, and the blue lines correspond to night. The red marks on each line indicate the absolute maxima on the L=5 to 15 $R_S$ interval. The shaded regions denote the scatter of each group of measurements.*

The nightside of Saturn is known to experience more frequent and intense injections than the dayside (Azari et al., 2018), so the difference in intensity there is to be expected. Because the L-shift successfully aligns the maxima of the mission-averaged data, we can safely assume that it is a more accurate representation of the ion drift paths. This improved alignment continues to appear between our modeled and compared half-orbit profiles, further confirming that the L-shift increases model verisimilitude.

## Acknowledgments

We are thankful to the institutions and personnel that made the Cassini mission and the MIMI instrument a success. We are also grateful to JHU/APL's Jon Vandegriff for assistance with data aggregation as well as Chris Paranicas and Todd Smith for their fruitful discussions. This work has been funded by NASA's Cassini Data Analysis Program under grant number: 80NSSC18K1234. The data presented here are available from the Planetary Plasma Interactions Node of NASA's Planetary Data System (https://pds-ppi.igpp.ucla.edu/ ).

## References


Azari, A. R., Liemohn, M. W., Jia, X., Thomsen, M. F., Mitchell, D. G., Sergis, N., et al. (2018). Interchange injections at Saturn: Statistical survey of energetic $H^+$ sudden flux intensifications. *J. Geophys. Res. Space Physics*, 123, 4692– 4711, doi:10.1029/2018JA025391.

Cassidy, T. A., and Johnson, R. E. (2010). Collisional spreading of Enceladus' neutral cloud. *Icarus*, *209*(2), 696-703, doi:10.1016/j.icarus.2010.04.010.

Carbary, J., Hedman, M., Hill, T., Jia, X., Kurth, W., Lamy, L., & Provan, G. (2018). The Mysterious Periodicities of Saturn: Clues to the Rotation Rate of the Planet. In K. Baines, F. Flasar, N. Krupp, & T. Stallard (Eds.), Saturn in the 21st Century (Cambridge Planetary Science, pp. 97-125). Cambridge: Cambridge University Press. doi:10.1017/9781316227220.005

Chen, Y., Hill, T. W., Rymer, A. M., and Wilson, R. J. (2010), Rate of radial transport of plasma in Saturn's inner magnetosphere, *J. Geophys. Res.*, 115, A10211, doi:10.1029/2010JA015412.

Clark, G., C. Paranicas, D. Santos-Costa, S. Livi, N. Krupp, D. G. Mitchell, E. Roussos, and W.- L. Tseng (2014). Evolution of electron pitch angle distributions across Saturn's middle magnetospheric region from MIMI/LEMMS. *Planetary and Space Science*, *104*, 18-28, doi:10.1016/j.pss.2014.07.004.

Delamere, P. A., Bagenal, F., Dols, V., and Ray, L. C. (2007), Saturn's neutral torus versus Jupiter's plasma torus, *Geophys. Res. Lett.*, 34, L09105, doi:10.1029/2007GL029437.

Dialynas, K., S. M. Krimigis, D. G. Mitchell, D. C. Hamilton, N. Krupp, and P. C. Brandt (2009), Energetic ion spectral characteristics in the Saturnian magnetosphere using Cassini/MIMI measurements, J. Geophys. Res., 114, A01212, doi:10.1029/2008JA013761.

Dialynas, K., Brandt, P. C., Krimigis, S. M., Mitchell, D. G., Hamilton, D. C., Krupp, N., and Rymer, A. M.(2013), The extended Saturnian neutral cloud as revealed by global ENA simulations using Cassini/MIMI measurements, *J. Geophys. Res. Space Physics*, 118, 3027– 3041, doi:10.1002/jgra.50295.

DiFabio, R. D. (2012). *Spatial and Temporal Variations of the Suprathermal (3-220 keV/e) Ion Composition in Saturn's Equatorial Magnetosphere* (Doctoral dissertation).

Dougherty, M. K., et al. (2004). The Cassini magnetic field investigation. In *The cassini-huygens mission* (pp. 331-383). Springer, Dordrecht, doi:10.1007/978-1-4020-2774-1_4.

Fillius, W., W. H. Ip, and C. E. McIlwain (1980), Trapped radiation belts of Saturn: First look, Science, 207, doi:10.1126/science.207.4429.425.

Fleshman, B. L., Delamere, P. A., and Bagenal, F. (2010), Modeling the Enceladus plume–plasma interaction, *Geophys. Res. Lett.*, 37, L03202, doi:10.1029/2009GL041613.

Fleshman, B. L., Delamere, P. A., Bagenal, F., and Cassidy, T. (2012), The roles of charge exchange and dissociation in spreading Saturn's neutral clouds, *J. Geophys. Res.*, 117, E05007, doi:10.1029/2011JE003996.

Gobet, F., Farizon, B., Farizon, M., Gaillard, M. J., Carré, M., Lezius, M., Scheier, P., & Märk, T. D. (2001). Total, partial, and electron-capture cross sections for ionization of water vapor by 20–150 keV protons. *Physical review letters*, *86*(17), 3751, doi:10.1103/PhysRevLett.86.3751.

Hodges, R. R., and Tinsley, B. A. (1981), Charge exchange in the Venus ionosphere as the source of the hot exospheric hydrogen, *J. Geophys. Res.*, 86( A9), 7649– 7656, doi:10.1029/JA086iA09p07649.

Hood, L. L. (1983), Radial diffusion in Saturn's radiation belts: A modeling analysis assuming satellite and ring E absorption, *J. Geophys. Res.*, 88( A2), 808– 818, doi:10.1029/JA088iA02p00808.

Horne, R. B., Meredith, N. P., Thorne, R. M., Heynderickx, D., Iles, R. H. A., and Anderson, R. R., Evolution of energetic electron pitch angle distributions during storm time electron acceleration to megaelectronvolt energies, *J. Geophys. Res.*, 108( A1), 1016, doi:10.1029/2001JA009165, 2003.

Johnson, R. E., and Strobel, D. F. (1982), Charge exchange in the Io torus and exosphere, *J. Geophys. Res.*, 87( A12), 10385– 10393, doi:10.1029/JA087iA12p10385.

Jurac, S., and Richardson, J. D. (2005), A self-consistent model of plasma and neutrals at Saturn: Neutral cloud morphology, *J. Geophys. Res.*, 110, A09220, doi:10.1029/2004JA010635.

Kennelly, T. J., Leisner, J. S., Hospodarsky, G. B., and Gurnett, D. A. (2013), Ordering of injection events within Saturnian SLS longitude and local time, *J. Geophys. Res. Space Physics*, 118, 832– 838, doi:10.1002/jgra.50152.

Kollmann, P. (2012). *Sources, sinks, and transport of energetic particles within Saturn's magnetosphere* (Doctoral dissertation, Techn. Univ. Carolo-Wilhelmina, Braunschweig).

Kollmann, P., E. Roussos, A. Kotova, J. F. Cooper, D. G. Mitchell, N. Krupp, and C. Paranicas (2015), MeV proton flux predictions near Saturn's D ring, J. Geophys. Res. Space Physics, 120, doi:10.1002/2015JA021621.

Kollmann, P., Roussos, E., Paranicas, C., Woodfield, E. E., Mauk, B. H., Clark, G., et al. (2018). Electron acceleration to MeV energies at Jupiter and Saturn. Journal of Geophysical Research: Space Physics, 123. https://doi.org/10.1029/2018JA025665

Krimigis, S. M., T. P. Armstrong, W. I. Axford, C. O. Bostrom, G. Gloekler, E. P. Keath, L. J. Lanzerotti, J. F. Carbary, D. C. Hamilton, and E. C. Roelof (1981), Low-energy charged particles in Saturn's magnetosphere- Results from Voyager 1, Science, 212, 225 – 231, doi:10.1126/science.212.4491.225.

Krimigis, S. M., T. P. Armstrong, W. I. Axford, C. O. Bostrom, G. Gloeckler, E. P. Keath, L. J. Lanzerotti, J. F. Carbary, D. G. Hamilton, and E. C. Roelof (1982), Low-energy hot plasma and particles in Saturn's magneto-sphere, Science, 215, 571–577, doi:10.1126/science.215.4532.571.

Krimigis, S. M., et al. (2004). Magnetosphere imaging instrument (MIMI) on the Cassini mission to Saturn/Titan. In *The Cassini-Huygens Mission* (pp. 233-329). Springer, Dordrecht, doi:10.1007/978-1-4020-2774-1_3.

Krupp, N., Kollmann, P., Mitchell, D., Thomsen, M., Jia, X., Masters, A., & Zarka, P. (2018). Global Configuration and Seasonal Variations of Saturn's Magnetosphere. In K. Baines, F. Flasar, N. Krupp, & T. Stallard (Eds.), Saturn in the 21st Century (Cambridge Planetary Science, pp. 126-165). Cambridge: Cambridge University Press. doi:10.1017/9781316227220.006

Lagg, A., Krupp, N., Woch, J., and Williams, D. J. (2003), In-situ observations of a neutral gas torus at Europa, *Geophys. Res. Lett.*, 30, 1556, doi:10.1029/2003GL017214.

Lai, H. R., Russell, C. T., Jia, Y. D., Wei, H. Y., and Dougherty, M. K. (2016), Transport of magnetic flux and mass in Saturn's inner magnetosphere, *J. Geophys. Res. Space Physics*, 121, 3050– 3057, doi:10.1002/2016JA022436.

Lejosne, S. and Kollmann, P. (2020), Radiation Belt Radial Diffusion at Earth and Beyond, SSR, SOI:10.1007/s11214-020-0642-6

Lindsay, B. G., and Stebbings, R. F. (2005), Charge transfer cross sections for energetic neutral atom data analysis, *J. Geophys. Res.*, 110, A12213, doi:10.1029/2005JA011298.

Lyons, L. R., and Thorne, R. M. (1972), Parasitic pitch angle diffusion of radiation belt particles by ion cyclotron waves, *J. Geophys. Res.*, 77( 28), 5608– 5616, doi:10.1029/JA077i028p05608.

Mauk, B. H., et al. (2005), Energetic particle injections in Saturn's magnetosphere, *Geophys. Res. Lett.*, 32, L14S05, doi:10.1029/2005GL022485.

Melin, H., Shemansky, D. E., and Liu, X. (2009). The distribution of atomic hydrogen and oxygen in the magnetosphere of Saturn. *Planetary and Space Science*, *57*(14-15), 1743-1753, doi:10.1016/j.pss.2009.04.014.

Morfill, G. E., Goertz, C. K., and Havnes, O. (1993), A dust-driven flux tube interchange instability, *J. Geophys. Res.*, 98( A2), 1435– 1442, doi:10.1029/92JA01951.

Nénon, Q., Sicard, A., Kollmann, P., Garrett, H. B., Sauer, S. P. A., & Paranicas, C. (2018). A physical model of the proton radiation belts of Jupiter inside Europa's orbit. Journal of Geophysical Research: Space Physics, 123, 3512–3532. https://doi.org/10.1029/2018JA025216

Paranicas, C., et al. (2008). Sources and losses of energetic protons in Saturn's magnetosphere. *Icarus*, *197*(2), 519-525, doi:10.1016/j.icarus.2008.05.011.

Paranicas, C., et al. (2010), Transport of energetic electrons into Saturn's inner magnetosphere, *J. Geophys. Res.*, 115, A09214, doi:10.1029/2010JA015853.

Paranicas, C., Thomsen, M. F., Achilleos, N., Andriopoulou, M., Badman, S. V., Hospodarsky, G., Jackman, C. M., Jia, X., Kennelly, K., Kollmann, P., Krupp, N., Louarn, P., Roussos, E., & Sergis, N. (2016), Effects of radial motion on interchange injections at Saturn. *Icarus*, *264*, 342-351, doi:10.1016/j.icarus.2015.10.002.

Persoon, A. M., et al. (2009), A diffusive equilibrium model for the plasma density in Saturn's magnetosphere, *J. Geophys. Res.*, 114, A04211, doi:10.1029/2008JA013912.

Richardson, J. D., Eviatar, A., McGrath, M. A., and Vasyliũnas, V. M. (1998), OH in Saturn's magnetosphere: Observations and implications, *J. Geophys. Res.*, 103( E9), 20245– 20255, doi:10.1029/98JE01127.

Richardson, J. D., and Sittler, E. C. (1990), A plasma density model for Saturn based on Voyager observations, *J. Geophys. Res.*, 95( A8), 12019– 12031, doi:10.1029/JA095iA08p12019.

Sánchez-Lavega, A. (2005). How long is the day on Saturn?. *Science*, *307*(5713), 1223-1224, doi:10.1126/science.1104956.

Saur, J., Schilling, N., Neubauer, F. M., Strobel, D. F., Simon, S., Dougherty, M. K., and Russell, C. T.(2008), Evidence for temporal variability of Enceladus' gas jets: Modeling of Cassini observations, *Geophys. Res. Lett.*, 35, L20105, doi:10.1029/2008GL035811.

Sibeck, D. G., McEntire, R. W., Lui, A. T. Y., Lopez, R. E., and Krimigis, S. M. (1987), Magnetic field drift shell splitting: Cause of unusual dayside particle pitch angle distributions during storms and substorms, *J. Geophys. Res.*, 92( A12), 13485– 13497, doi:10.1029/JA092iA12p13485.

Smith, H. T., Johnson, R. E., Perry, M. E., Mitchell, D. G., McNutt, R. L., and Young, D. T. (2010), Enceladus plume variability and the neutral gas densities in Saturn's magnetosphere, *J. Geophys. Res.*, 115, A10252, doi:10.1029/2009JA015184.

Southwood, D. J., and Kivelson, M. G. (1987), Magnetospheric interchange instability, *J. Geophys. Res.*, 92( A1), 109– 116, doi:10.1029/JA092iA01p00109.

Teolis, B. D., Perry, M. E., Hansen, C. J., Waite, J. H., Porco, C. C., Spencer, J. R., & Howett, C. J. (2017). Enceladus plume structure and time variability: comparison of Cassini observations. *Astrobiology*, *17*(9), 926-940, doi:10.1089/ast.2017.1647.

Thomsen, M. F., Roussos, E., Andriopoulou, M., Kollmann, P., Arridge, C. S., Paranicas, C. P., Gurnett, D. A., Powell, R. L., Tokar, R. L., and Young, D. T. (2012), Saturn's inner magnetospheric convection pattern: Further evidence, *J. Geophys. Res.*, 117, A09208, doi:10.1029/2011JA017482.

Van Allen, J. A., M. F. Thomsen, B. A. Randall, R. L. Rairden, and C. L. Grosskreutz (1980), Saturn's magnetosphere, rings and inner satellites, Science, 207, 415–421, doi:10.1126/science.207.4429.415.

Vandegriff, J., DiFabio, R., Hamilton, D., Kusterer, M., Manweiler, J., Mitchell, D., Paranicas, C., Roussos, E., and LaVallee, D. (2018), Cassini/MIMI Instrument Data User Guide.